Improved collision handling of elastic solids in SPH using a contact force model

Dinesh Adepu[a,*], Prabhu Ramachandran[a]

[a]*Department of Aerospace Engineering, Indian Institute of Technology Bombay, Powai, Mumbai 400076*

Abstract

Modeling of collision between elastic solids involves deformation of bodies and the interaction with other bodies. Classically, SPH is used for both, but, this does not allow one to incorporate friction and also subjects the solids to unphysical interaction when the bodies are nearby but not in actual contact. In the current work, we incorporate an efficient contact force model into a variant of updated-Lagrangian SPH to model the interaction between elastic solids. This approach models friction as well as eliminates the spurious interaction between nearby bodies. The current model is validated with several numerical examples, involving collision between two and multiple elastic solids, with and without friction. These results compare well with FEM, analytical, and experimental studies. The model is easy to incorporate in any updated-Lagrangian SPH scheme. We provide a fully open-source implementation along with a reproducible manuscript.

Keywords: Elastic solids collision, Frictional contact, SPH, Transport Velocity Formulation

1. Introduction

The collision of arbitrary solid bodies occurs everywhere around us. Apart from the elastic collision of bodies, other important examples include surface erosion, waterjet machining [1], and machining processes [2] to note a few. It

*Corresponding author

Email addresses: adepu.dinesh.a@gmail.com (Dinesh Adepu), prabhu@aero.iitb.ac.in (Prabhu Ramachandran)

is important to be able to simulate such problems accurately. One of the ways to study the dynamics of such bodies is by assuming the bodies to be rigid, as done in the discrete element method (DEM) ([3]). However, this does not consider any elastic or elastic-plastic deformations of these colliding bodies. In these cases either finite element methods (FEM) [4] or meshless methods such as material point method[5] or smoothed particle hydrodynamics (SPH) [6] can be used. In this context meshless methods, such as the SPH method, are advantageous when modeling large deformation of solids as they do not suffer from issues such as mesh entanglement.

The SPH method is a meshless numerical method originally proposed by Gingold and Monaghan [6] and Lucy [7] to model astrophysics problems. It has been extensively applied to simulate problems involving fluids [8, 9], structural dynamics [10, 11], fluid-structure interaction [12, 13], granular physics [14, 15] among other areas. Monaghan [16] provides a detailed review of SPH and its applications. Modeling of elastic solids in SPH was first proposed by Libersky and Petschek [17], where the authors studied the high-speed impact problems.

Despite SPH being applied to many areas, it suffers from tensile instability [18] as well as the inhomogeneous particle distribution. The tensile instability problem has given rise to the total Lagrangian SPH [19, 20, 21], where the derivatives of particle properties are computed in the reference configuration using the deformation gradient. The updated Lagrangian approach is used by Gray et al. [22] and Monaghan [23] where an artificial stress term is introduced to control instabilities. Many other variants of the updated Lagrangian SPH have been proposed. Godunov SPH [24] utilizes a Riemann solver to reduce the usage of artificial viscosity and a new equation of state is formulated to solve the tensile instability problem. Dyka and Ingel [25] uses two sets of particles, where one set of particles stress is computed, and the other set of particles are used for the evolution of other properties, through which the tensile instability has been overcome. Zhang et al. [26] extended the transport velocity formulation (TVF) of Adami et al. [27] to structural dynamics problems and free-surface fluid mechanics problems. Here the particles are moved with a transport velocity rather than the momentum velocity to ensure a more homogenous particle distribution. This approach also solves the tensile instability problem. Adepu and Ramachandran [28] have proposed corrected transport velocity formulation (CTVF), where the missing terms in the formulation of Adami et al. [27] are added and the method is extended to work with free-surfaces and solid mechan-

ics problems. The CTVF can handle higher Poisson ratios [28] than Gray et al. [22] formulation. In the current work, we use the CTVF formulation to model the elastic dynamics of a solid body.

SPH has been successful in modeling the collision between the elastic as well as elastic-plastic solids [22, 29]. This approach does not consider friction between the colliding solids. Another problem is that the model generates spurious forces on bodies which are moving close to each other (within the influence radius of the SPH particles) but not actually interacting. In order to mitigate this, Yan et al. [30] introduces the interfacial SPH scheme, where the SPH forces are computed only within each body but the interaction between two bodies is computed using a repulsive force inspired from ABAQUS. Vyas et al. [31] has modeled the interaction between a rigid body with an elastic solid, using a penalty-based contact force model. Mohseni-Mofidi et al. [32] use a contact model in order to simulate the collision between non-smooth rigid bodies with elasto-plastic targets. In both [31] and [32] the friction between the rigid body and target is considered.

In the current work, the collision between elastic solids is modeled using a penalty-based contact force model. Unlike the approach of [30], the proposed contact force model can handle friction between the solids as well. The bodies themselves are elastic and this is simulated using the CTVF SPH method [28]. The penalty-based force considered here is the one proposed by Mohseni-Mofidi et al. [32]. In the original model proposed by [32], the contact force is between a primary body and a secondary body. In [32], the primary body is usually treated as the rigid body and the body on which the erosion is simulated is treated as secondary. It is not clear what would happen if both bodies were elastic or if there is no clear way to distinguish between a primary and secondary body. We explore these questions in the present work. The work of Mohseni-Mofidi et al. [32] takes inspiration from that of Vyas et al. [31] where too there is a clear distinction between primary and secondary bodies. Vyas et al. [31] also consider the collision between a rigid and elastic body. In the present work we only implement the collision model of [32] due to its simplicity. The model proposed by Vyas et al. [31] is more complex to implement. Several examples are simulated to validate the current scheme, ranging from simulations compared with FEM, analytical results as well as experimental. Finally, in the interest of reproducibility and easier ability for researchers to build on this work, our code is open source and can be found at `https://gitlab.com/pypr/collision_sph`. We use the `automan` package [33] to automate all the results generated in the current

manuscript.

This paper is structured as follows. In section 2, we demonstrate the numerical method utilized to model the dynamics of collision of frictional elastic solids. In section 3, we present the contact force model used to resolve the collision among the elastic bodies. The results are provided in section 4, where different problems from the literature are simulated to show the capability of the current solver. Problems with collision involving two and multiple frictional and friction-less elastic solids are simulated.

2. SPH model for structural dynamics

2.1. Discrete governing equations

The governing equations of CTVF[28] scheme including the new contact force term are:

$$\frac{\tilde{d}\rho_a}{dt} = \sum_{b\in A} \frac{m_b}{\rho_b} \left(\rho_a \, \tilde{\mathbf{u}}_{ab} \; + \; (\rho \, (\tilde{\mathbf{u}} \; - \; \mathbf{u}))_{ab}\right) \; \cdot \nabla_a W_{ab}, \tag{1}$$

$$\frac{\tilde{d}\mathbf{u}_a}{dt} = -\sum_{b\in A} m_b \left[\left(\frac{p_a}{\rho_a^2}+\frac{p_b}{\rho_b^2}\right)\mathbf{I} - \left(\frac{\boldsymbol{\sigma}_a^{'}}{\rho_a^2}+\frac{\boldsymbol{\sigma}_b^{'}}{\rho_b^2}+\Pi_{ab}\mathbf{I}\right)\right]\cdot\nabla_a W_{ab} + \mathbf{g}_a + \frac{1}{m_a}\sum_{b\in B}\mathbf{F}^{\text{cont}}_{a\leftarrow b}. \tag{2}$$

In the above equations, the density, mass, pressure, deviatoric stress, momentum velocity, and transport velocity of particle a are denoted by ρ_a, m_a, p_a, $\boldsymbol{\sigma}_a^{'}$, $\mathbf{u}_a$ and $\tilde{\mathbf{u}}_a$ respectively. $\mathbf{g}_a$, is the acceleration due to gravity and $\mathbf{F}_a^{cont}$ is the force acting on particle a due to

contact with the other elastic bodies which will be discussed in section 3. The pressure p_a is evaluated using an equation of state:

$$p_a = K\left(\frac{\rho_a}{\rho_0} - 1\right). \tag{3}$$

Where, $K = \rho_0 \, c_0^2$ is bulk modulus of the body, with $c_0 = \sqrt{\frac{E}{3(1-2\nu)\rho_0}}$ is speed of sound, while ρ_0 as the initial density of the particles. Here, E and ν are Young's modulus and Poisson ratio of the body. The modified material derivative $(\frac{\tilde{d}}{dt})$ is given as,

$$\frac{\tilde{d}}{dt} = \frac{\partial}{\partial t} + \tilde{u}_j \frac{\partial}{\partial x_j}. \tag{4}$$

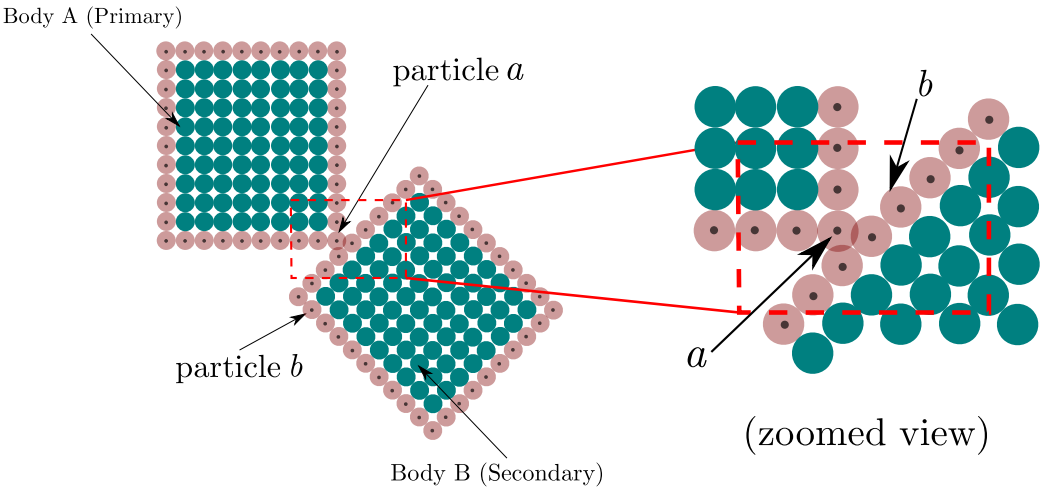

Figure 1: Bodies under collision which are divided into primary and secondary.

The additional artificial viscosity term Π_{ab} [34] in the momentum eq. (2) is to maintain the stability of the numerical scheme, given as,

$$\Pi_{ab} = \begin{cases} \frac{-\alpha h_{ab} \bar{c}_{ab} \phi_{ab}}{\bar{\rho}_{ab}} & \mathbf{u}_{ab} \cdot \mathbf{r}_{ab} < 0, \\ 0 & \mathbf{u}_{ab} \cdot \mathbf{r}_{ab} \geq 0, \end{cases} \tag{5}$$

where,

$$\phi_{ab} = \frac{\mathbf{u}_{ab} \cdot \mathbf{r}_{ab}}{r_{ab}^2 + 0.01 h_{ab}^2}, \tag{6}$$

where $\mathbf{r}_{ab} = \mathbf{r}_a - \mathbf{r}_b$, $r_{ab} = |\mathbf{r_{ab}}|$, $\mathbf{u}_{ab} = \mathbf{u}_a - \mathbf{u}_b$, $h_{ab} = (h_a + h_b)/2$, $\bar{\rho}_{ab} = (\rho_a + \rho_b)/2$, $\bar{c}_{ab} = (c_a + c_b)/2$, α is the artificial viscosity parameter, and h_a is the smoothing length.

Deviatoric stress $\boldsymbol{\sigma}_a$ evolution follows the Hooke's stress as,

$$\frac{d\sigma'_{ij}}{dt} = 2G(\dot{\epsilon}_{ij} - \frac{1}{3}\dot{\epsilon}_{kk}\delta_{ij}) + \sigma'_{ik}\Omega_{jk} + \Omega_{ik}\sigma'_{kj}, \tag{7}$$

where, G is the shear modulus, $\dot{\epsilon}_{ij}$ is the strain rate tensor, $\dot{\epsilon}_{ij} = \frac{1}{2}\left(\frac{\partial u_i}{\partial x_j} + \frac{\partial u_j}{\partial x_i}\right)$, and $\Omega_{ij} = \frac{1}{2}\left(\frac{\partial u_i}{\partial x_j} - \frac{\partial u_j}{\partial x_i}\right)$ is the rotation tensor. Here, SPH discretization of the gradient of velocity is given as, $\nabla \mathbf{u}_a = -\sum_{b \in A} \frac{m_b}{\rho_b}(\mathbf{u}_a - \mathbf{u}_b) \otimes (\nabla_a W_{ab})$, where $\otimes$ is the outer product.

The position of the particle is moved using the transport velocity, given as,

$$\frac{d\mathbf{r}_a}{dt} = \tilde{\mathbf{u}}_a, \tag{8}$$

where, $\mathbf{r}_a$ is the position of the particle a. The transport velocity $\tilde{\mathbf{u}}_a$ is computed with,

$$\tilde{\mathbf{u}}_a(t + \Delta t) = \mathbf{u}_a(t) + \Delta t \, \frac{\tilde{d}\mathbf{u}_a}{dt} + \left(\frac{d\mathbf{u}_a}{dt}\right)_{\mathrm{c}} \Delta t. \tag{9}$$

$\left(\frac{d\mathbf{u}_a}{dt}\right)_{\mathrm{c}}$ is the homogenization acceleration in eq. (9) and is computed with an iterative particle shifting technique (IPST) [35]. In IPST, at each time instant a shifting vector of particle a is computed as

$$\delta r_a^k = U_{\mathrm{IPST}} \, \Delta t \, \sum_{b \in A} (V_b \, \mathbf{n}_{ab} \, W_{ab}), \tag{10}$$

where k is the iteration number, $k = (1, 2, 3, \dots)$. U_{IPST} is taken to be four times the maximum velocity of the particles, can possibly achieve in a given simulation, found from the numerical experiments. The particles are then moved as,

$$\mathbf{r}_a^{k+1} = \mathbf{r}_a^k + \delta \mathbf{r}_a^k. \tag{11}$$

New particle positions are found until the convergence criterion is achieved, defined as,

$$|\max(\chi_a^k) - \overline{\chi_a^k}| \leq \epsilon, \tag{12}$$

where

$$\chi_a^k = h^2 \sum_{b \in A} W_{ab}^k. \tag{13}$$

Here $\overline{\chi_a^k}$ is set to the maximum value of all the particles at initial configuration, which corresponds to the free surface particle. We find setting the value to the maximum gives better tensile instability control.

Using the initial ($\mathbf{r}_a^0$) and final ($\mathbf{r}_a^K$) positions at the given time instant, $\left(\frac{d\mathbf{u}_a}{dt}\right)_{\mathrm{c}}$ is computed as,

$$\left(\frac{d\mathbf{u}_a}{dt}\right)_{\mathrm{c}} = 2 \, \frac{\mathbf{r}_a^K - \mathbf{r}_a^0}{\Delta t^2}, \tag{14}$$

where $\mathbf{r}_a^K$ is the final position of the particle a.

The particle shifting force needs to be adjusted near the free surface, this is due to the lack of support for the particles near the free-surface. In order to do so we first identify the particles on the free surface, which starts with the computation of $\mathbf{n}_a^*$,

$$\mathbf{n}_a^* = \sum_{b \in A} -\frac{m_b}{\rho_b} \nabla_a W_{ab}, \tag{15}$$

where, particles with the magnitude of $\mathbf{n}_a^*$ less than $\frac{1}{4h_a}$, is set to zero else we normalize. Next, we smooth $\mathbf{n}_a^*$ using an SPH approximation,

$$\hat{\mathbf{n}}_a = \sum_{b \in A} \frac{m_b}{\rho_b} \mathbf{n}_b^* W_{ab}. \tag{16}$$

Finally, we compute the normals by normalizing $\hat{\mathbf{n}}_a$,

$$\mathbf{n}_a = \frac{\hat{\mathbf{n}}_a}{||\hat{\mathbf{n}}_a||}. \tag{17}$$

The PST is treated near the free surface by adjusting the increment in the position near the free surface. We employ a new variable, h_b, initialized to smoothing length h. For particles near the free surface, it is readjusted to a value such that its kernel support is up to the closest boundary particle. This algorithm identifies the particles close to the free surface. By using the identified free surface particles, and particles near the free surface, the increment of the position is adjusted as,

$$\delta \mathbf{r}_a = \begin{cases} 0 & \text{if free-surface,} \\ \delta \mathbf{r}_a - (\delta \mathbf{r}_a \cdot \mathbf{n}_a)\mathbf{n}_a & \text{if } h_b < h, \\ \delta \mathbf{r}_a & \text{if } h_b = h. \end{cases} \tag{18}$$

2.2. Time integration

The time integration follows a kick-drift-kick scheme: first we move the velocities of the particles to half time step by using the acceleration at the n^{th} time step,

$$\begin{aligned} \mathbf{u}_a^{n+\frac{1}{2}} &= \mathbf{u}_a^n + \frac{\Delta t}{2} \left(\frac{\tilde{d}\mathbf{u}_a}{dt} \right)^n, \\ \tilde{\mathbf{u}}_a^{n+\frac{1}{2}} &= \mathbf{u}_a^{n+\frac{1}{2}} + \frac{\Delta t}{2} \left(\frac{d\mathbf{u}_a}{dt} \right)_c^n. \end{aligned} \tag{19}$$

The time derivatives of density and deviatoric stresses are calculated using the eq. (1) and eq. (7) by utilizing the velocities at n+$\frac{1}{2}$ time step. The density, deviatoric stresses and particle position are updated by,

$$\rho_a^{n+1} = \rho_a^n + \Delta t \left(\frac{\tilde{d}\rho_a}{dt} \right)^{n+\frac{1}{2}}, \tag{20}$$

$$\boldsymbol{\sigma}_a^{'\,n+1} = \boldsymbol{\sigma}_a^{'\,n} + \Delta t \left(\frac{\tilde{d}\boldsymbol{\sigma}_a^{'}}{dt} \right)^{n+\frac{1}{2}}, \tag{21}$$

$$\mathbf{r}_a^{n+1} = \mathbf{r}_a^n + \Delta t \; \tilde{\mathbf{u}}_a^{n+1}. \tag{22}$$

Finally, the momentum velocity is updated to the n+1 time step

$$\mathbf{u}_a^{n+1} = \mathbf{u}_a^{n+\frac{1}{2}} + \frac{\Delta t}{2} \left(\frac{\tilde{d}\mathbf{u}_a}{dt} \right)^{n+1}. \tag{23}$$

For the numerical stability, the time step is set based on the CFL criterion,

$$\Delta t \leq 0.25 \left(\frac{h}{c_0 + |U|} \right), \tag{24}$$

and $|U|$ is the maximum velocity magnitude.

3. Contact algorithm

In the current work we have utilized the contact force model proposed by Mohseni-Mofidi et al. [32]. The force acting on a particle a of body A due to the interaction with the particles of body B can be resolved into a normal and tangential component. The normal force component is utilised to make sure that the particles of different body do not penetrate into each other, while the tangential component is used to model the friction between the interacting solids. According to Mohseni-Mofidi et al. [32], we divide the bodies under interaction into primary and secondary bodies, as shown in fig. 1. The normal force ($\boldsymbol{F}_a^n$) on particle a due to the interaction with the particles b of body B is computed as,

$$\mathbf{F}_a^n = k_r \delta_{n^c}^a \mathbf{n}_a^c. \tag{25}$$

Here, the overlap $\delta_{n^c}^a$ is computed using

$$\delta_{n^c}^a = \Delta x - d_a, \tag{26}$$

where,

$$d_a = \frac{\sum_{b=1}^{\mathrm{NP}^b} \left(\mathbf{n}_a^c \cdot \mathbf{r}_{ab}\right) \frac{m_b}{\rho_b} W_{ab}}{\sum_{b=1}^{\mathrm{NP}^b} \frac{m_b}{\rho_b} W_{ab}}, \tag{27}$$

and the normal contact vector $\mathbf{n}_a^c$ is computed using

$$\hat{\mathbf{n}}_a^c = \frac{\sum_{b=1}^{\mathrm{NP}^b} \frac{\mathbf{r}_{ab}}{r_{ab}} \frac{m_b}{\rho_b} W_{ab}}{\sum_{b=1}^{\mathrm{NP}^b} \frac{m_b}{\rho_b} W_{ab}}, \tag{28}$$

$$\mathbf{n}_a^c = \frac{\hat{\boldsymbol{n}}_a^c}{||\hat{\boldsymbol{n}}_a^c||}. \tag{29}$$

With Δx being the initial spacing between the particles, k_r is the normal spring stiffness coefficient. Note that while computing the overlap of particle a with the body B we have computed an effective overlap, rather than per particle interaction. This effectively is able to model the interaction between non smooth surfaces in contrast with particle-particle force computation.

3.1. Tangential force computation

We associate a tangential spring attached to particle i and body B to compute the tangential force, which initially has a magnitude of zero ($|\Delta \boldsymbol{l}_a| = 0$). And the tangential spring is activated when the particle comes into contact with body B. The tangential force is history-dependent. The contact friction force is proportional to the tangential spring displacement, which is integrated over the contact time as

$$\mathbf{F}_a^{t^{n+1}} = -k_f \Delta \boldsymbol{l}_a^{n+1} = -k_f \left[\left(\Delta \boldsymbol{l}_a^n + \mathbf{v}_{ab}^{n+1} \Delta t\right) \cdot \mathbf{t}_a^{n+1}\right] \mathbf{t}_a^{n+1}, \tag{30}$$

where Δt is the time step, $\mathbf{v}_{ab} = \mathbf{v}_a - \mathbf{v}_b$ is the relative velocity of the primary particle a with respect to the closest secondary particle b, and k_f is the tangential spring stiffness coefficient. The tangential unit vector is computed by,

$$\mathbf{t}_a = \frac{\mathbf{v}_{ab} - (\mathbf{v}_{ab} \cdot \mathbf{n}_a^c)\mathbf{n}_a^c}{\left|\mathbf{v}_{ab} - (\mathbf{v}_{ab} \cdot \mathbf{n}_a^c)\mathbf{n}_a^c\right|}. \tag{31}$$

The tangential force is coupled to the normal force through the Coulomb's law,

$$\mathbf{F}_a^t = \min(\mu|\mathbf{F}_a^n|, |\mathbf{F}_a^t|)\ \frac{\mathbf{F}_a^t}{|\mathbf{F}_a^t|}. \tag{32}$$

This allows us to impose the sliding friction condition between the interacting solids. Finally, the total force acting on the particle a due to the interaction with body B is:

$$\mathbf{F}_a^{\text{cont}} = \mathbf{F}_a^n + \mathbf{F}_a^t \tag{33}$$

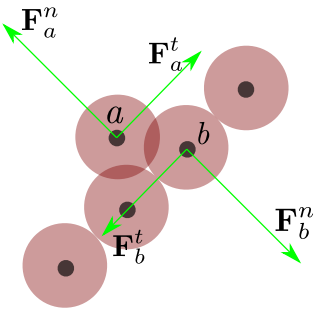

Figure 2: Force transfer to the secondary particles b from the primary body particle a

An equal and opposite force of the same magnitude is applied to the closest secondary particle b of a as shown in fig. 2,

$$\mathbf{F}_b^{\text{cont}} = -\mathbf{F}_a^{\text{cont}}. \tag{34}$$

The current contact force model is sensitive towards the primary body chosen to compute the forces, i.e., the force acting on the particles is not the same when the primary bodies are interchanged. In the current work we have explored the behaviour of the current contact force model when different bodies are chosen as primary and secondary. Simulations such as, a rectangular solid sliding down an inclined plane, and a symmetric collision between elastic solids are two examples, where we have investigated how the bodies would behave when different bodies are chosen as primary.

4. Results and discussion

4.1. Curved interface

The collision of two circular elastic solids is considered as the first test case. Figure 3 shows the initial configuration where the left disc is initially

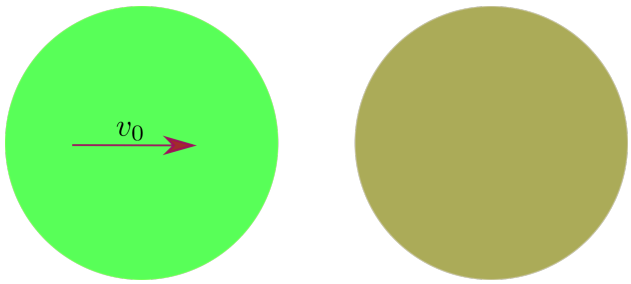

Figure 3: Collision between two circular elastic discs. The left disc moves towards the right disc with a constant velocity v_0, while the right disc is at rest.

allowed to move towards the right with a velocity of 20 $\mathrm{m\,s^{-1}}$. While no velocity is imposed on the right disc. The radius of each disk is 0.4 m, and made of Aluminium, whose material properties are shown in table 1. No friction and gravity is assumed in the current case. A particle spacing of 0.01 m is used, resulting in a 4779 number of particles per disc. The numerical parameters utilized in the current example are shown in table 2.

Quantity	Values
E, Young's modulus	72 GPa
ν, Poisson's ratio	0.3
ρ, density	2785 $\mathrm{kg\,m^{-3}}$
μ, friction coefficient	0
Time of simulation	4 ms
gravity $[g_x, g_y, g_z]$	$[0.0, 0.0, 0.0]$

Table 1: Material parameters used for the impact of curved interface problem.

Figure 4 shows the snapshots of particles of the circular disc under contact by the present approach including the stress (σ_{xx}) field at times $t = 0.0, 1.8, 4$ ms. From the figure, we can see that the current numerical scheme is able to reproduce smooth stress fields. The elastic discs are initially in stress free state, and once the bodies collide, the left disc transfers its momentum to the right. Since the discs are elastic, the total momentum is not transferred, and the left disc will not come to a halt but rather starts moving with the free vibration of the disc.

Figure 5 presents the time histories of the velocity of the center of mass of both the discs in comparison with the results by FEM solver presented in

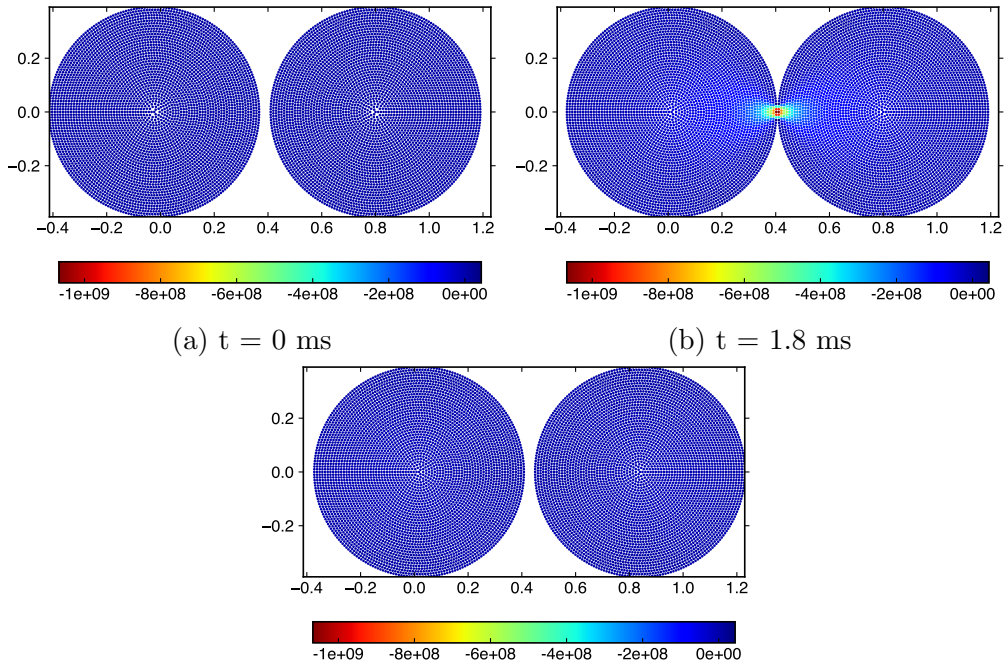

(a) t = 0 ms

(b) t = 1.8 ms

(c) t = 4 ms

Figure 4: The stress field of the elastic discs at three different time instants through the collision.

Quantity	Values
δx, Resolution	0.01
$h/\Delta x$, Smoothing length factor	1
α, artificial viscosity	1
β, artificial viscosity	0
k_r, Normal stiffness coefficient	10^{10}
k_f, Tangential stiffness coefficient	10^9

Table 2: Numerical parameters used for the impact of curved interface problem.

[30]. The rebound the velocity of the bodies with the current scheme is in good match with the FEM result.

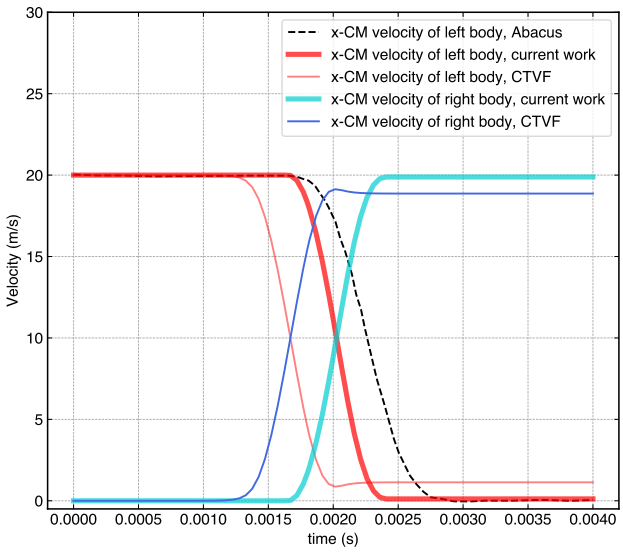

Figure 5: Time history of the x component of velocity of center of mass's of the left and the right disc, and compared with the numerical results produced using FEM, CTVF. The Young's modulus of the disc is taken as E=72 GPa.

We check if the elastic disk behave as a rigid disk with an increase in Young's modulus and is able to retrieve the rigid velocity. We expect the right disk to achieve the velocity of 20 $\mathrm{m\,s^{-1}}$ as the Young's modulus is increased. Figure 6 shows the variation of the final velocity of the right disc with Young's modulus, where we can see that the proposed model is behaving as expected.

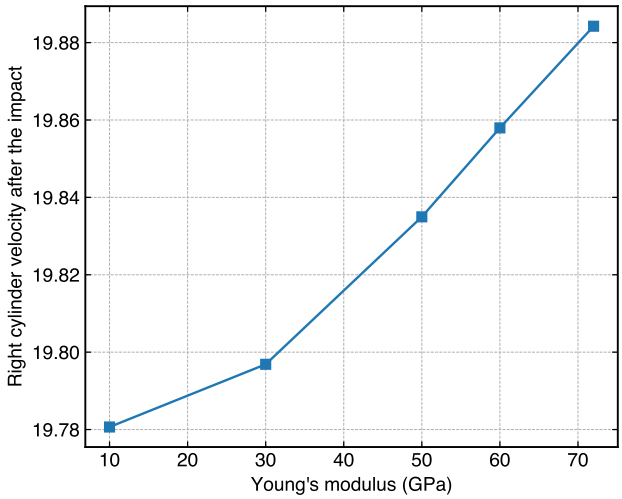

Figure 6: Variation of the x-velocity of the center of mass with Young's modulus of the disc.

4.2. Flat interface

In the current section, we test our solver in handling collision between two elastic solids, where the collision front is flat in shape. The model is shown in fig. 7. Both the solids are of the same size, 0.2 m in length and 0.1 m in height. The material is the same as in the circular interface problem (section 4.1) and can be found in table 1, while the numerical parameters are listed in table 3. A particle spacing of 0.0025 m is used, resulting in 3321 particles per body.

Figure 7: Collision between two rectangular elastic solids, where, the left solid is allowed to move towards the right solid with a constant velocity v_0, while the right solid is at rest.

Figure 8 shows the velocity of the center of mass of both the bodies using current scheme along with the formulation of Gray et al. [22] and with FEM results provided by Yan et al. [30]. From the fig. 8 we can see that rebound velocities match well with the FEM results provided, as well as the

Quantity	Values
$h/\Delta x$, Smoothing length factor	1
α, artificial viscosity	1
β, artificial viscosity	0
k_r, Normal stiffness coefficient	10^{11}
k_f, Tangential stiffness coefficient	10^9

Table 3: Numerical parameters used for the impact of linear interface problem.

interaction between the bodies start when their physical boundaries have come into contact, in contrast to SPH, where the bodies interact when the other body is in its smoothing length influence. The rebound velocity of the current scheme is matches well with FEM result. Since the body is elastic after the collision, both the bodies move with the base oscillation amplitude which is the reason for the left body to not achieve absolute zero velocity. The current scheme results are better than the Adepu and Ramachandran [28] SPH model.

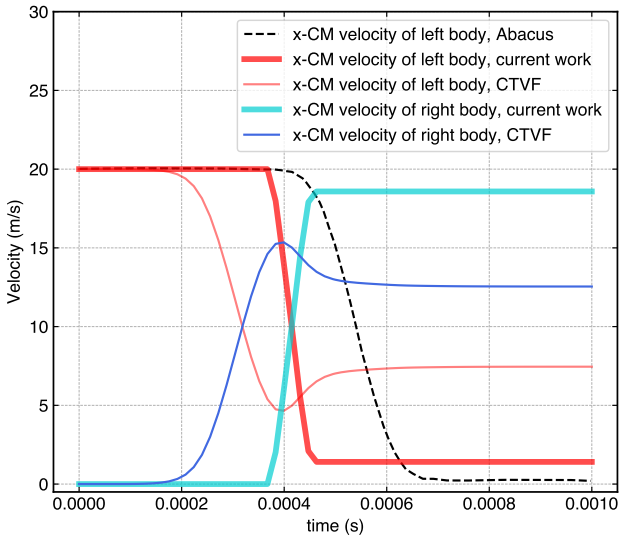

Figure 8: Time history of the x component of the center of mass's velocity of the left and the right rectangular bodies, and compared with the numerical results produced using FEM, SPH.

4.3. Colliding rubber rings

This test applies the current solver in modeling large deformation solids under collision. We consider the collision between two elastic rubber rings. This benchmark is simulated by various works in SPH literature, such as in Gray et al. [22], Adepu and Ramachandran [28], Zhang et al. [26].

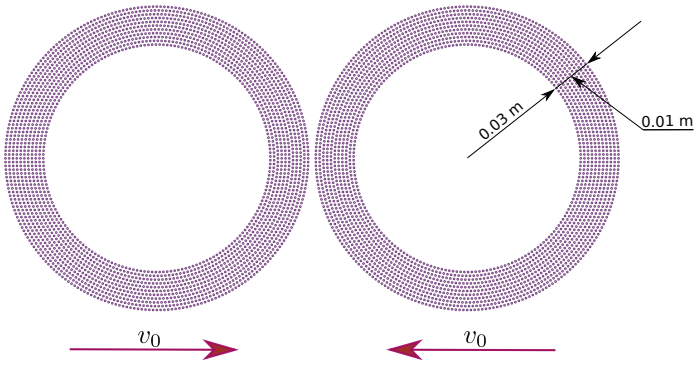

Figure 9: Schematic sketch of the initial setup of colliding rubber rings.

The initial positioning, as well as the dimensions of the rings, are shown in fig. 9. Both rings are made of the same material, whose material properties are listed in table 4, and the numerical parameters in table 5, respectively. The initial relative velocity at which the rings collide is $v_0 = 0.12c_0$ m s^{-1}.

Quantity	Values
E, Young's modulus	10 MPa
ν, Poisson's ratio	0.47
ρ, density	1200 kg m^{-3}
μ, friction coefficient	0.0
Time of simulation	0.016 s
Resolution, δx	0.001 m
Smoothing length factor, $h/\Delta x$	1.3
gravity $[g_x, g_y, g_z]$	$[0.0, 0.0, 0.0]$

Table 4: Material parameters used for modeling the impact of elastic rubber rings.

The evolution of the rings is shown in fig. 10, we can see from the figure that the current model has reproduced a stable and smooth stress field. The

Quantity	Values
α, artificial viscosity	1
β, artificial viscosity	0
k_r, Normal stiffness coefficient	10^7
k_f, Tangential stiffness coefficient	10^5

Table 5: Numerical parameters used for modeling the impact of elastic rubber rings.

rings are stress free before the collision, as shown in fig. 10a. Throughout the simulation phase, while the rings are colliding, the kinetic energy of the rings is transferred into elastic and vice versa. At the maximum deformation, the elastic energy stored in the rings is maximum. After that, both the rings bounce off and start to separate. Further, we can see the rings being under tension as well as compression, while it is deforming in fig. 10e. The results are consistent with other numerical methods proposed by Gray et al. [22] and Zhang et al. [26].

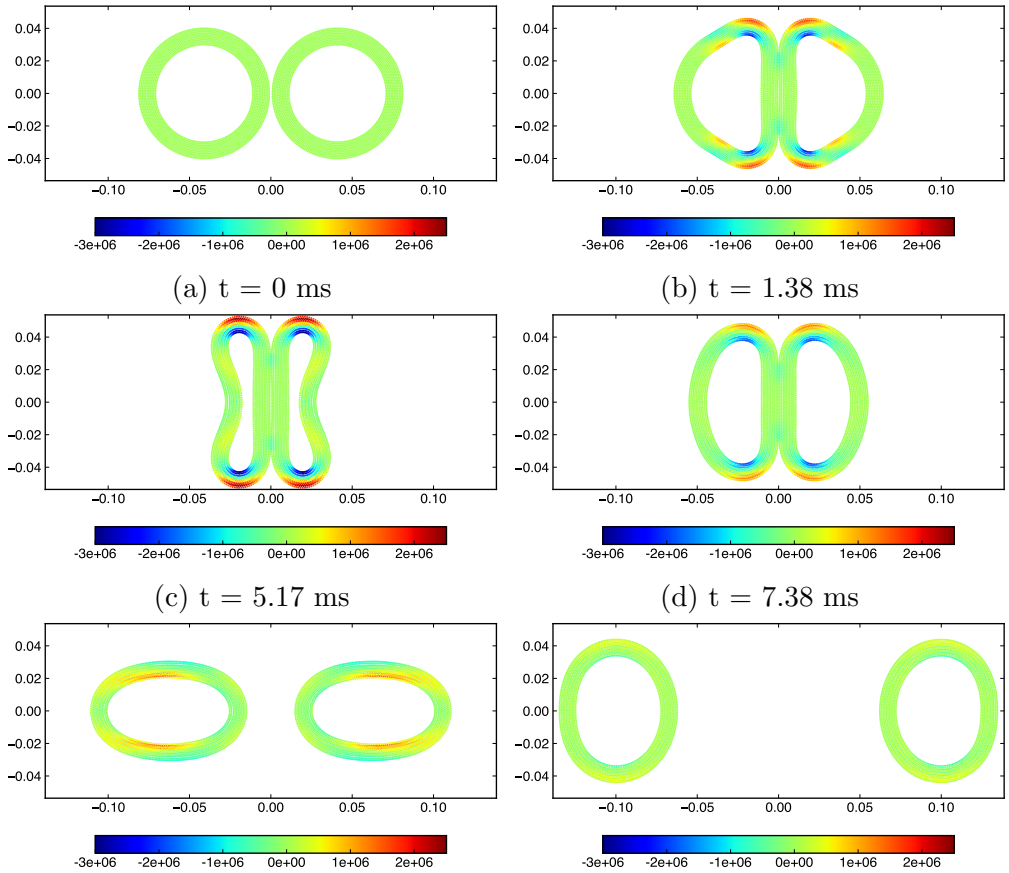

(a) t = 0 ms (b) t = 1.38 ms

(c) t = 5.17 ms (d) t = 7.38 ms

(e) t = 11.462 ms (f) t = 15.4 ms

Figure 10: Snapshots of particle positions with color indicating the stress field (σ_{xx}) solved by the current solver.

4.4. Near miss of two solids

In this section, we simulate two elastic solids which are not touching are moved towards each other with a constant velocity. We show that the current model is able to eliminate the unphysical interaction arises due to the conventional SPH which is due to the physical influence of the particles at the boundary. We expect no change in the velocity of the elastic solids as they pass by. We show that with the current model no interaction exists when the elastic solids are physically not touching, and no variation in their path is found. As a qualitative validation the particle plots is shown and for quantitative validation, variation of the velocity of the center of mass of the elastic body with time is considered.

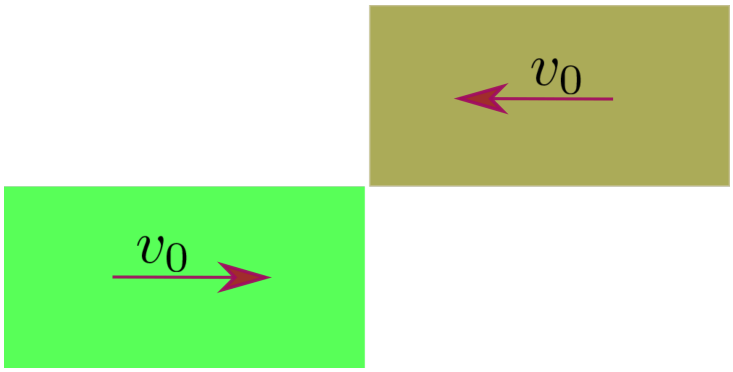

Figure 11: Schematic of the two elastic solids which are placed close to each other and allowed to move at a constant velocity v_0.

The dimensions of the elastic bodies under consideration are as follows, the length and height are 0.2 m and 0.1 m, respectively. Both bodies are made of density 1200 $\mathrm{kg\,m^{-3}}$, Young's modulus of 10 MPa and Poisson's ratio of 0.4. The schematic is shown in fig. 11. The left body is allowed to move to the right in the x-direction with a velocity of $v_0 = 20\ \mathrm{m\,s^{-1}}$, and the right body with $v_0 = -20\ \mathrm{m\,s^{-1}}$. A particle spacing of dx = 0.0025 m is used, which results in 3321 particles per single body. We have turned off the particle shifting in the current test case as no deformation of the bodies is expected.

Figure 12 shows the snapshots of bodies at multiple time instants simulated using the formulation of Adepu and Ramachandran [28]. From Figure 12 we can see that the bodies interact with each other though they are not touching physically, this is because in SPH the particles at the boundaries have an influence radius exceeding its material boundary. Because of the

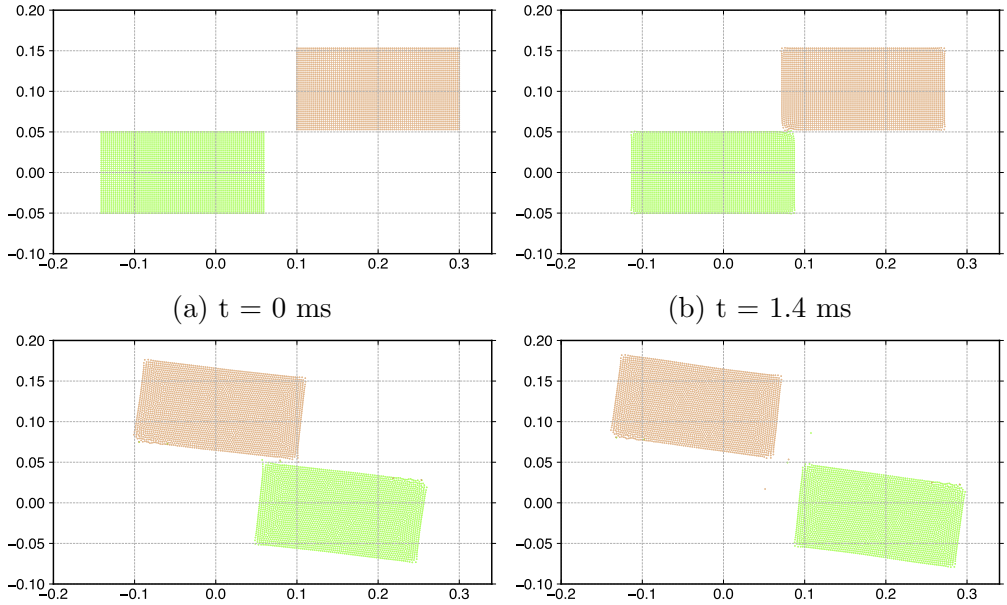

(a) t = 0 ms (b) t = 1.4 ms

(c) t = 10 ms (d) t = 12 ms

Figure 12: Snapshots of the bodies passing close by when simulated with CTVF.

interaction, shear stresses develop, which results in strain in the body as well as it deviates from its path. Figure 13 shows the snapshots of bodies when simulated with the current contact force model with the current SPH formulation. From fig. 13, we can clearly see that the bodies don't interact and pass freely without any deformations or path divergence. Figure 14 shows a quantitative validation by considering the time history of the velocity of the center of mass in the x and y-direction. From fig. 14 we can see that the velocity of the left body, as well as the right body, is constant throughout the time. While a velocity in the y-direction is induced while simulated using Adepu and Ramachandran [28] formulation. Hence the current scheme is successful in modeling the free moment of elastic solids passing close by each other.

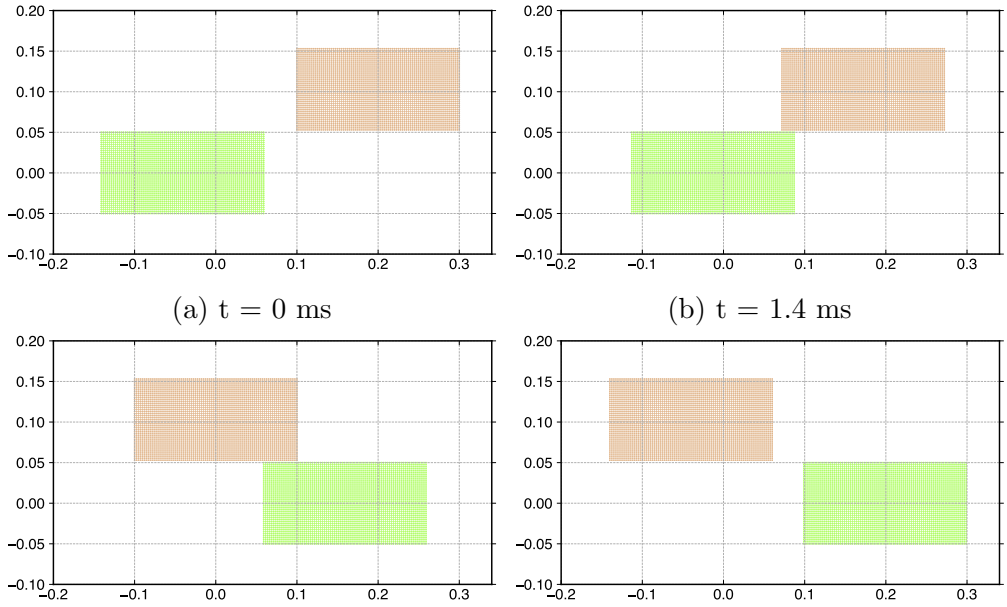

(a) t = 0 ms (b) t = 1.4 ms

(c) t = 10 ms (d) t = 12 ms

Figure 13: Snapshots of the bodies passing close by when simulated with current solver.

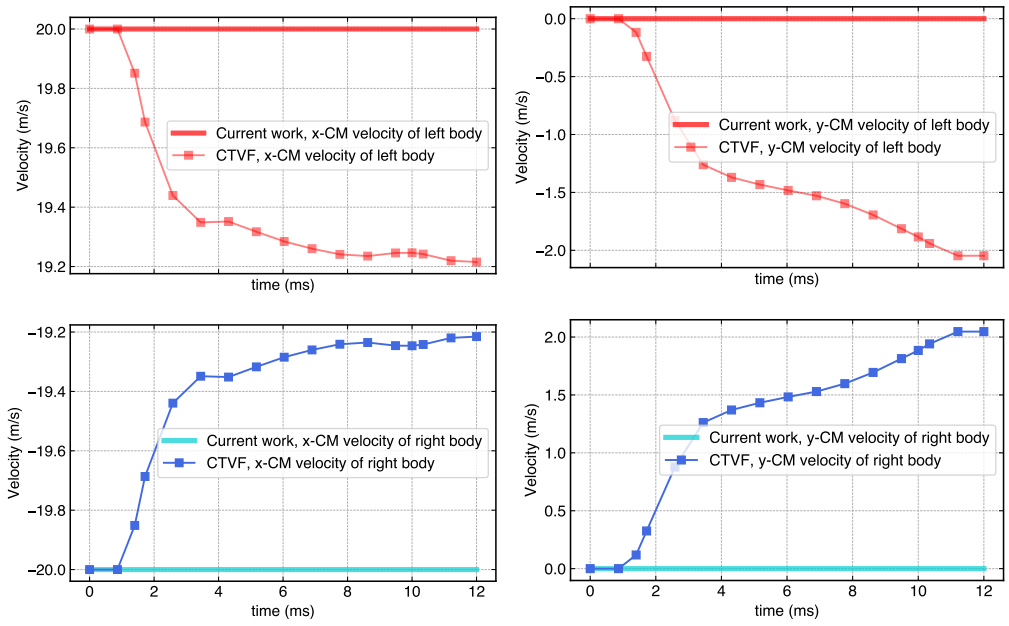

Figure 14: Time variation of the x-component and y-component of the velocity of the center of mass of the freely moving rectangular solids when simulated using the CTVF and the current solver.

4.5. Elastic solid sliding on a slope

In the current problem, we test if the current scheme models the friction between the elastic solids accurately. The free sliding of an elastic solid on a frictional inclined plane is studied. The initial placement of the elastic solid is shown in fig. 15.

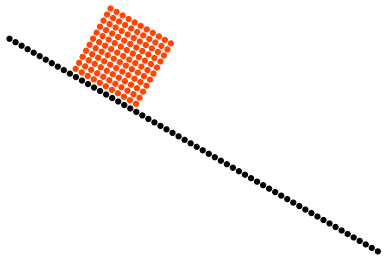

Figure 15: Schematic of an elastic body sliding on a frictional slope.

The dimensions of the elastic solid involved are as follows. An elastic solid of length 0.1 m and width 0.1 m is initially placed at zero velocity on an inclined plane at an angle of 30 degrees. The material properties are as follows: An Young's modulus of 10 MPa with a Poisson ratio of 0.3975 is considered. We have turned the particle homogenization off in the current problem, as the particle shifting effects are negligible. A stiffness coefficient k_r of 10^{10} in eq. (25) is used. From the analytical solution, we have the evolution of velocity as follows,

$$\mathbf{v}(t) = (\mu \boldsymbol{g} \sin(\theta) - \boldsymbol{g} \cos(\theta))t. \tag{35}$$

We consider three different frictional coefficients, $\mu = 0.2, 0.3, 0.4$ while modeling the sliding of the elastic solid. Snapshots at four time instants are depicted in fig. 16, corresponding to the frictional coefficient of 0.3. From fig. 16 we can see that the elastic solid slides without any oscillations. Figure 17 presents the time history of the velocity of center of mass of the elastic body along with the corresponding theoretical solution obtained by frictional coefficients of $\mu = 0.2$, 0.3, and 0.4. From fig. 17, the reproduced velocity is in good agreement with the corresponding theoretical solution for all the time.

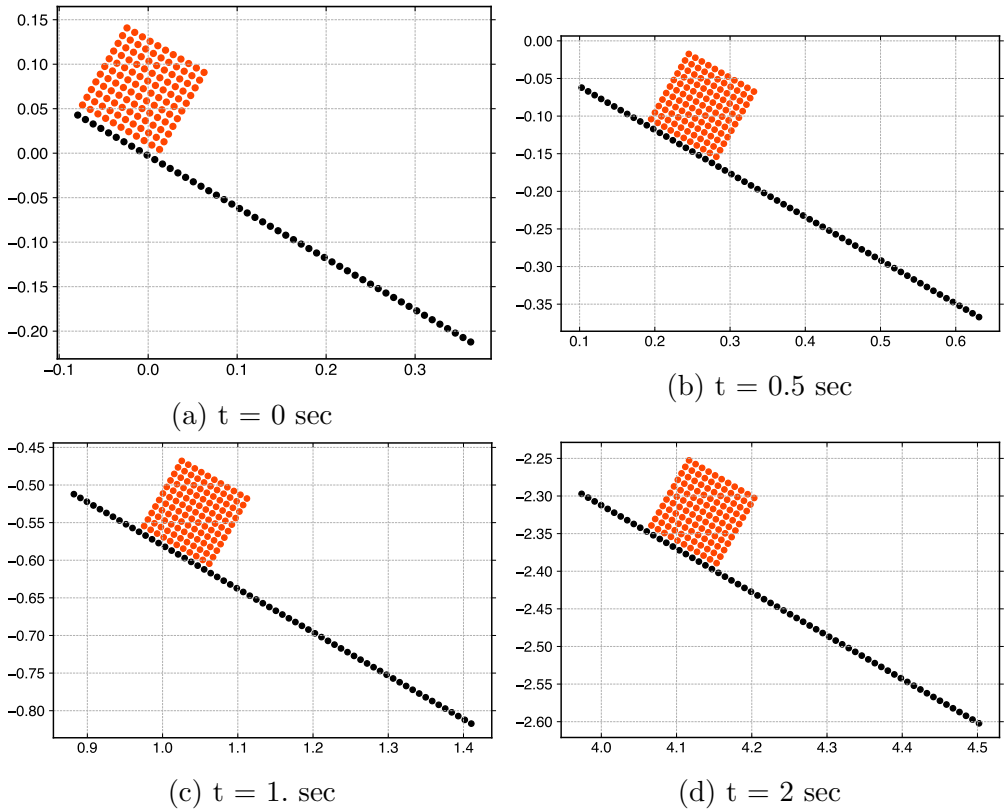

Figure 16: Snapshots of the elastic solid sliding on an inclined plane at four time steps, where, the friction coefficient between the body and the plane is taken as 0.3.

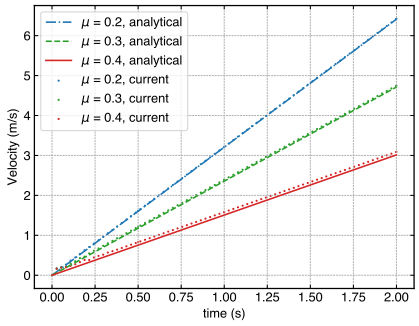

Figure 17: Time histories of the velocity of the elastic solid while sliding on an inclined plane for three frictional coefficients, plotted against the analytical solution.

4.6. Circular elastic body rolling on a plane

In the current section, the motion of a 2D elastic cylinder rolling on a frictional inclined plane is carried out. The theoretical and computational model are shown in fig. 18. In addition to section 4.5, the current problem will be helpful in testing the frictional part of the current formulation. A

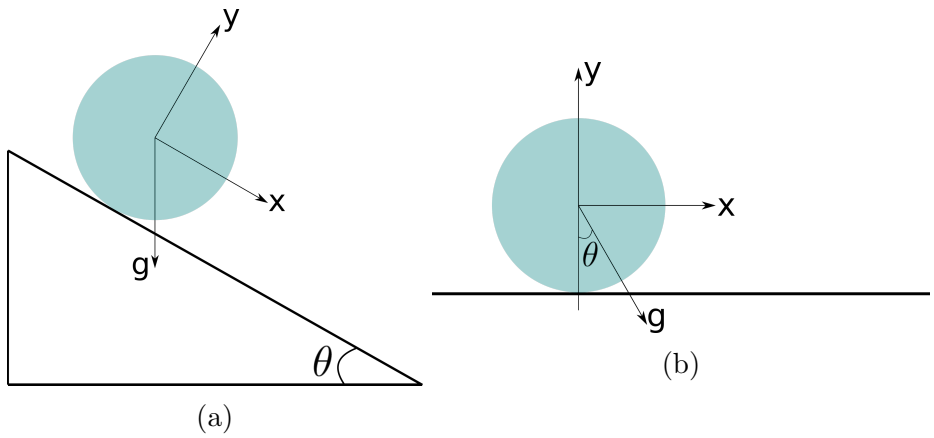

Figure 18: The rolling body problem: (a) theoretical description (b) numerical model.

total of two coefficient of friction μ values are simulated. One with a slip case ($\mu = 0.3$) and with $\mu = 0.6$ corresponding to stick case, where the inclination of the plane is chosen to be $\theta = \pi/3$. Table 6 shows the material properties along with numerical parameters utilized in the current scheme. The analytical solution of the movement of the center of the circular body for different frictional coefficients is given as

$$x_{cm}(t) = \begin{cases} x_0 + \frac{1}{2}\, g\, t^2\, (\sin(\theta) - \mu \cos(\theta)) & \tan\theta > 3.5\mu, \\ x_0 + \frac{1}{3}\, g\, t^2\, \sin(\theta) & \tan\theta \leq 3.5\mu. \end{cases} \tag{36}$$

Here, $g = 9.81$ is the magnitude of acceleration due to gravity.

Figure 19 and Figure 20 shows the snapshots of the cylinder at two different time instants along with the scaled velocity vectors for friction coefficients $\mu = 0.3$ and 0.6 respectively. Finally, fig. 21 and fig. 22 depicts the x position of the center of mass of the cylinder along with time for a slip and stick case. From these figures, we can see that the current scheme agrees well with the analytical solution.

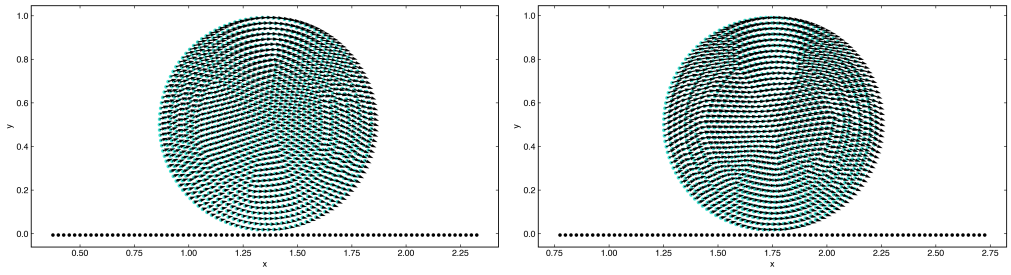

(a) (b)

Figure 19: Snapshot of a rolling cylinder with the velocity vectors at two time steps for a friction coefficient of 0.3, corresponding to a slip case.

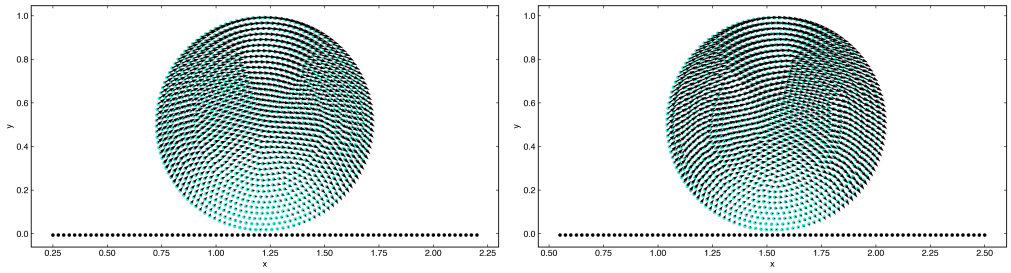

(a) (b)

Figure 20: Snapshot of a rolling cylinder with the velocity vectors at two time steps for a friction coefficient of 0.6, corresponding to a stick case.

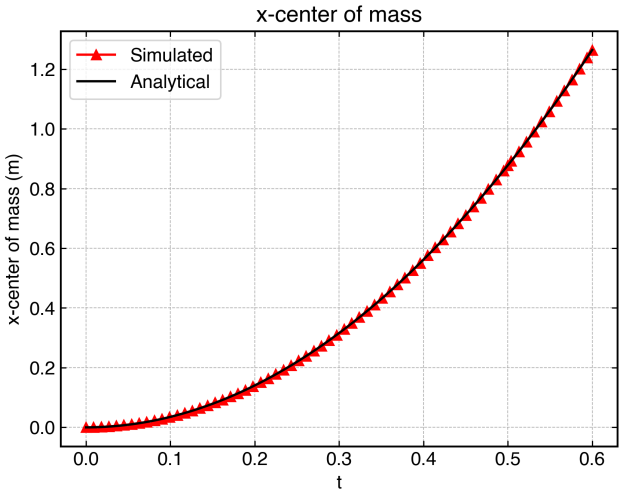

Figure 21: Time variation of the x-component of the center of mass of the circular cylinder for a friction coefficient of 0.3.

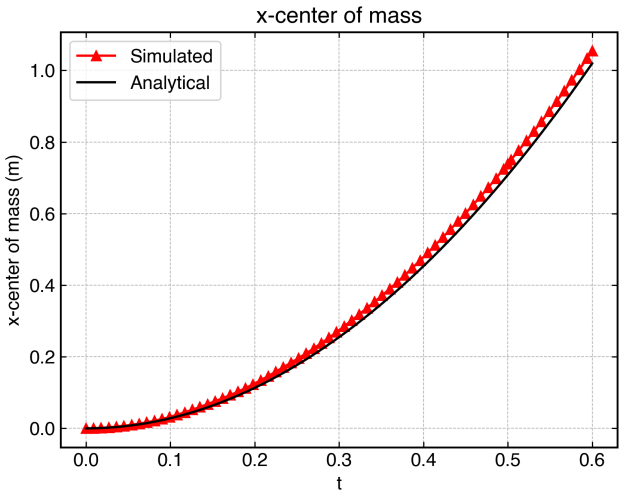

Figure 22: Time variation of the x-component of the center of mass of the circular cylinder for a friction coefficient of 0.6.

Quantity	Values
E, Young's modulus	10 MPa
ν, Poisson's ratio	0.3975
ρ, density	1200 kg m^{-3}
μ, friction coefficient	0.3 & 0.6
Time of simulation	0.6 s
Resolution, δx	0.0025 m
Smoothing length factor, $h/\Delta x$	1.3
gravity $[g_x, g_y, g_z]$	$[g\ \sin(\theta), g\ \cos(\theta), 0.0]$
α, artificial viscosity	1
β, artificial viscosity	0
k_r, Normal stiffness coefficient	10^7
k_f, Tangential stiffness coefficient	10^5

Table 6: Numerical parameters and material properties for the rolling circular cylinder.

4.7. A rigid sphere hitting a wall at different impact angles

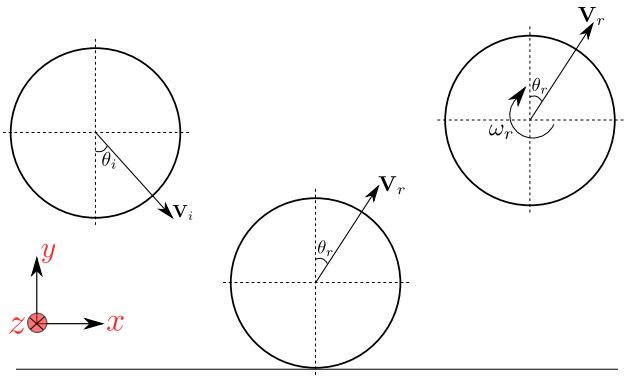

Figure 23: 3d rigid body rebound schematic

In the current example, we simulate the impact of a 3D sphere on a wall at different incident angles, where the experimental evaluation is done by Thornton et al. [36]. The model description is shown in fig. 23. The sphere is assumed to be rigid and the material properties as well as the numerical parameters used are displayed in table 7. The sphere is impacted on the wall by varying the incident angles (θ_i) keeping the magnitude of the velocity constant, 5 m s^{-1}.

Quantity	Values
E, Young's modulus	70 GPa
ν, Poisson's ratio	0.3
ρ, density	2650 kg m^{-3}
μ, friction coefficient	0.1
Time of simulation	0.25 ms
Resolution, δx	0.00153 m
Smoothing length factor, $h/\Delta x$	1.0
gravity $[g_x, g_y, g_z]$	$[0.0, -9.81, 0.0]$
k_r, Normal stiffness coefficient	10^7
k_f, Tangential stiffness coefficient	10^5

Table 7: Numerical parameters and material properties for sphere impacting a wall.

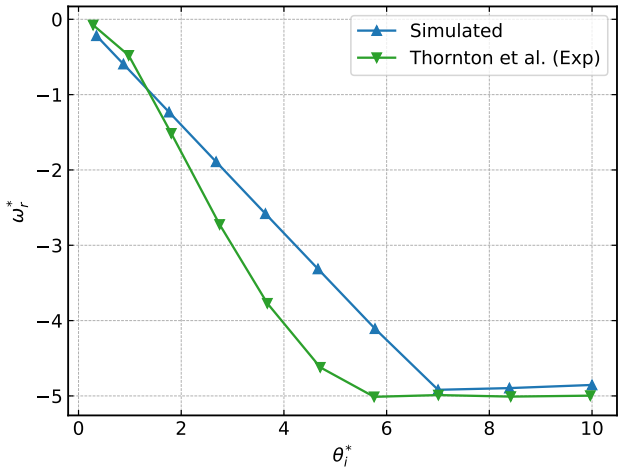

Figure 24: The plot of the variation of ω_r^* with θ_i^* of the impacting sphere simulated with the current numerical scheme, compared with the experimental result by Thornton et al. [36].

Figure 24 depicts the variation of the non-dimensional angular velocity ω_r^* against the non-dimensional incident angle θ_i^*, where θ^* and ω_r^* are defined as

$$\theta_i^* = \frac{2\tan(\theta_i)}{(1+e_n)\mu}, \tag{37}$$

$$\omega_r^* = \frac{2\,R\,\omega_r}{(1+e_n)\,\mu\,V_{ni}}, \tag{38}$$

respectively. Here, ω_r corresponds to the z-component of the angular velocity vector. The simulated results are compared to the experimental results by Thornton et al. [36]. From the fig. 24, we can see that the current solver is able to replicate the original behavior to an acceptable approximation. We observe that the variation of the ω_r^* with θ_i^* to be linear with the current solver whereas the experimental result to be a nonlinear, this may be due to the usage of the linear force model in the current scheme.

4.8. Stress wave propagation in granular media

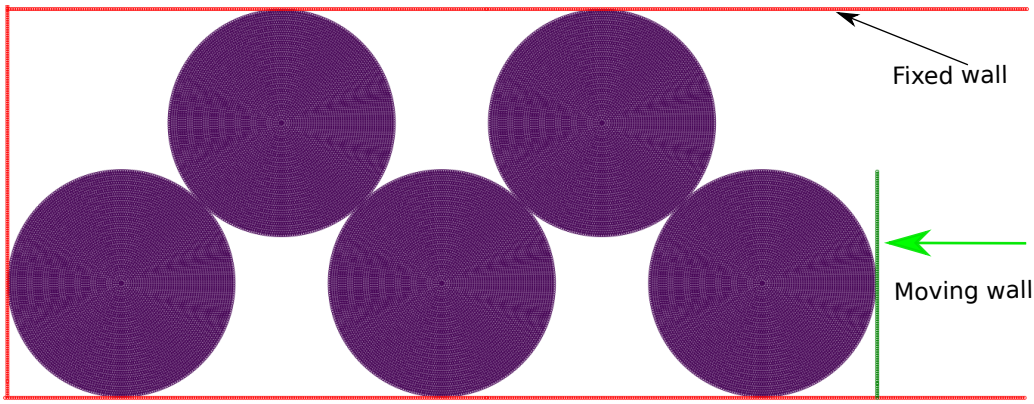

Figure 25: Schematic of the initial placement of the frictional granular media including the impactor and walls

So far, we have modeled the collision between two bodies, in the current section, we study the collision among multiple bodies. The elastic wave propagation in a granular media is carried out, and whose experimental study was executed by Guilkey et al. [37]. To our knowledge this problem has not yet done in SPH literature yet. We consider five identical disks placed at an angle of 45 degrees, allowed to be impacted by a striker from right with a velocity 5.6 $\mathrm{m\,s^{-1}}$ in horizontal direction as depicted in fig. 25. Each granular disk has a radius of 50 mm, which are initially placed such that just touching. A particle spacing of 1.25 mm is used, which results in 7830 particles per disk. The rigid box are modelled as rigid surfaces. The material parameters of the

disc as well as the numerical parameters used in the numerical simulation are listed in table 8. Figure 26 shows the particle plots of the granular discs

Quantity	Values
K, Bulk modulus	102 GPa
G, Shear modulus	72 GPa
ρ, density	1900 $\mathrm{kg\,m^{-3}}$
gravity $[g_x, g_y, g_z]$	$[0.0, 0.0, 0.0]$
k_r, Normal stiffness coefficient	1.75×10^{11}
k_f, Tangential stiffness coefficient	5×10^{10}
μ, Friction coefficient	0.5

Table 8: Material and numerical parameters used for the stress wave propagation problem.

with the stress fringes from the experiment [37], and the simulation carried in the present study, and from the numerical study of de Vaucorbeil and Nguyen [38], where the simulation is carried out using a total Lagrangian material point method (TLMPM). The snapshots of the current work are taken at time 0.2 ms, while the results of experimental and TLMPM result correspond to the time at 0.12 ms. This is due to the initial placement of the discs in the current work and the stress fringes being sensitive to initial placement. Here, the stress fringes in the experimental work are evaluated using photo-elasticity. While, in the numerical work, the fringes are generated by plotting σ_f, computed as:

$$\sigma_f = 1 - \sin^2(f(\sigma_1 - \sigma_3)), \tag{39}$$

where f is a optical parameter which controls the fringe density, taken as $\pi/0.07$ $\mathrm{G\,Pa^{-1}}$. The difference in the in-plane principal stress is computed using,

$$\sigma_1 - \sigma_3 = 2R = \sqrt{4\tau_{xy}^2 + (\sigma_x - \sigma_y)^2} \tag{40}$$

From the qualitative comparison of the stress fringes in the granular discs of the current scheme with the experimental as well as the numerical result of TLMPM, the current scheme fringes are smooth and are similar to the experimental result.

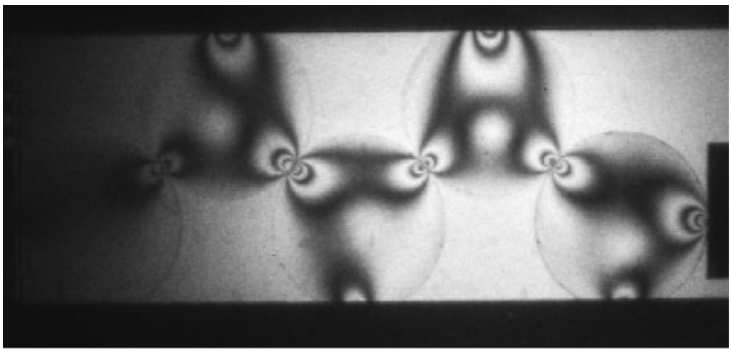

(a)

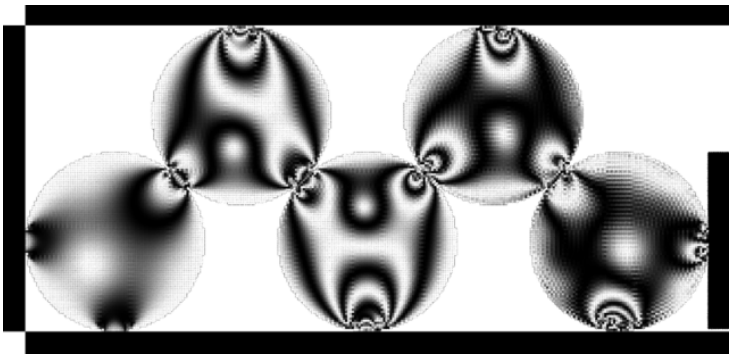

(b)

(c)

Figure 26: Stress fringes of the granular discs from (a) experiment [37], (b) TLMPM [38] (c) Current work

4.9. Primary secondary analysis

In the current section we have studied the dependence of the behaviour of current contact force model on the variation of different bodies being primary. We have considered the following examples:

- Collision between symmetric bodies
- Circular cylinder rolling down an inclined plane
- Square solid sliding down an inclined plane
- Impact of a 3D sphere against a target wall.

Figure 27 depicts the variation of velocity or position of the elastic bodies involved in above cases. From fig. 27 we can see that the velocities of the elastic solids in a symmetric collision are invariant to the primary body chosen. While, considering the wall as primary in rolling cylinder, and sliding solid case, the error is more compared to the body being taken as primary. And in the case of granular particle impacting a wall, the angular velocity of the granular particle deviates from the experimental result when the wall being the primary body. With these results, we conclude that body with more curvature is advised to take as primary.

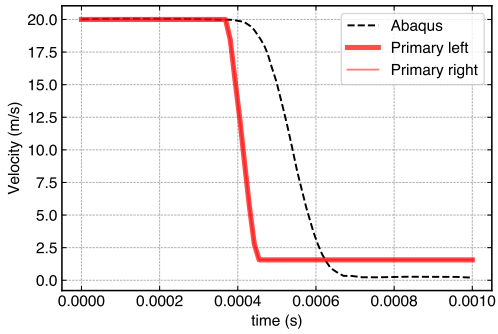

(a) Collision between a flat interface solids.

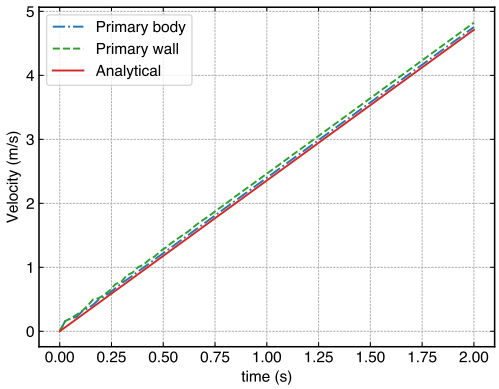

(b) An elastic body sliding down an inclined plane

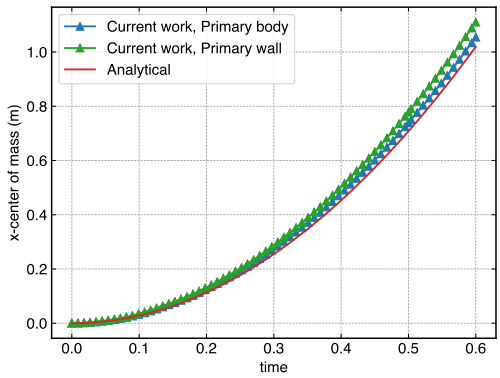

(c) A circular cylinder rolling on an inclined plane

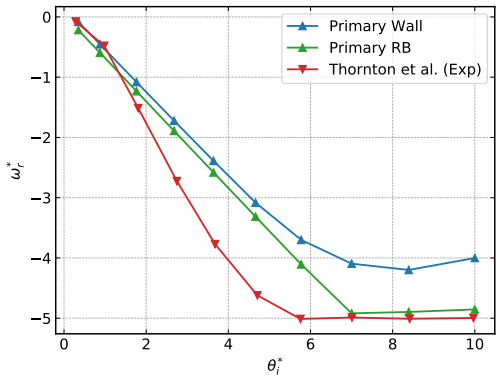

(d) Variation of the angular velocity with respect to the incident theta.

Figure 27

5. Conclusions

In this paper we have demonstrated a simple approach to effectively handle the collision between elastic solids modeled using an updated Lagrangian SPH model. A contact force model is used to handle the collision between bodies. A surface aware spring based contact force is used to handle the collision between bodies. This effectively allows us to model collision and friction accurately. In addition this eliminates any spurious forces that are commonly seen with SPH when two bodies are nearby but not in actual contact. The contact force model utilized in the current work is sensitive towards the primary and the secondary body chosen. A careful analysis is carried out to understand which body is to be considered as primary among the colliding solids, and it is found that choosing the body with the highest curvature as the primary body gives the best results. Further, we have made our implementation open-source.

It has been demonstrated that the current model is able to predict the post collision behaviour of the colliding bodies by simulating collision between flat, and curved interfaces in two and three dimensions. A sliding elastic body is simulated to test the frictional part of the contact model. Finally, the full scale model is applied to model the stress propagation in granular discs for the first time in SPH. The results compare well with those of FEM as well as analytical studies.

A non-linear contact force model can be implemented in the future work. The current work can be easily extended to the modeling of collision between elastic and elastic-plastic bodies. Also, the collision between the bodies undergoing breakage can be easily captured with the current framework.

References

1. Natarajan, Y., Murugesan, P.K., Mohan, M., Khan, S.A.L.A.. Abrasive water jet machining process: A state of art of review. *Journal of Manufacturing Processes* 2020;49:271–322.

2. Islam, M.R.I., Bansal, A., Peng, C.. Numerical simulation of metal machining process with eulerian and total lagrangian sph. *Engineering Analysis with Boundary Elements* 2020;117:269–283.

3. Zhan, L., Peng, C., Zhang, B., Wu, W.. A surface mesh represented discrete element method (smr-dem) for particles of arbitrary shape. *Powder Technology* 2021;377:760–779.

4. Rodrigues, G., Weber, H., Driemeier, L.. Elastic and plastic collision comparison using finite element method. *International Journal of Mechanical and Mechatronics Engineering* 2019;13(5):354–358.

5. Sulsky, D., Chen, Z., Schreyer, H.L.. A particle method for history-dependent materials. *Computer methods in applied mechanics and engineering* 1994;118(1-2):179–196.

6. Gingold, R.A., Monaghan, J.J.. Smoothed particle hydrodynamics: theory and application to non-spherical stars. *Monthly notices of the royal astronomical society* 1977;181(3):375–389.

7. Lucy, L.B.. A numerical approach to the testing of the fission hypothesis. *The astronomical journal* 1977;82:1013–1024.

8. Dalrymple, R.A., Knio, O.. Sph modelling of water waves. In: *Coastal dynamics' 01*. 2001:779–787.

9. Shao, S., Lo, E.Y.. Incompressible sph method for simulating newtonian and non-newtonian flows with a free surface. *Advances in water resources* 2003;26(7):787–800.

10. Randles, P., Libersky, L.D.. Smoothed particle hydrodynamics: some recent improvements and applications. *Computer methods in applied mechanics and engineering* 1996;139(1-4):375–408.

11. Dong, X., Liu, G., Li, Z., Zeng, W.. A smoothed particle hydrodynamics (sph) model for simulating surface erosion by impacts of foreign particles. *Tribology International* 2016;95:267–278.

12. Khayyer, A., Gotoh, H., Falahaty, H., Shimizu, Y.. An enhanced isph–sph coupled method for simulation of incompressible fluid–elastic structure interactions. *Computer Physics Communications* 2018;232:139–164.

13. He, J., Tofighi, N., Yildiz, M., Lei, J., Suleman, A.. A coupled wc-tl sph method for simulation of hydroelastic problems. *International Journal of Computational Fluid Dynamics* 2017;31(3):174–187.

14. Bui, H.H., Fukagawa, R., Sako, K., Ohno, S.. Lagrangian meshfree particles method (sph) for large deformation and failure flows of geomaterial using elastic–plastic soil constitutive model. *International journal for numerical and analytical methods in geomechanics* 2008;32(12):1537–1570.

15. Bui, H.H., Nguyen, G.D.. Smoothed particle hydrodynamics (sph) and its applications in geomechanics: From solid fracture to granular behaviour and multiphase flows in porous media. *Computers and Geotechnics* 2021;138:104315.

16. Monaghan, J.J.. Smoothed particle hydrodynamics and its diverse applications. *Annual Review of Fluid Mechanics* 2012;44:323–346.

17. Libersky, L.D., Petschek, A.G.. Smooth particle hydrodynamics with strength of materials. In: *Advances in the free-Lagrange method including contributions on adaptive gridding and the smooth particle hydrodynamics method*. Springer; 1991:248–257.

18. Swegle, J.W., Hicks, D.L., Attaway, S.. Smoothed particle hydrodynamics stability analysis. *Journal of computational physics* 1995;116(1):123–134.

19. Bonet, J., Kulasegaram, S.. Alternative total lagrangian formulations for corrected smooth particle hydrodynamics (csph) methods in large strain dynamic problems. *Revue Européenne des Éléments Finis* 2002;11(7-8):893–912.

20. Vignjevic, R., Reveles, J.R., Campbell, J.. Sph in a total lagrangian formalism. *CMC-Tech Science Press-* 2006;4(3):181.

21. Belytschko, T., Guo, Y., Kam Liu, W., Ping Xiao, S.. A unified stability analysis of meshless particle methods. *International Journal for Numerical Methods in Engineering* 2000;48(9):1359–1400.

22. Gray, J.P., Monaghan, J.J., Swift, R.. Sph elastic dynamics. *Computer methods in applied mechanics and engineering* 2001;190(49-50):6641–6662.

23. Monaghan, J.J.. Sph without a tensile instability. *Journal of computational physics* 2000;159(2):290–311.

24. Sugiura, K., Inutsuka, S.i.. An extension of godunov sph ii: Application to elastic dynamics. *Journal of Computational Physics* 2017;333:78–103.

25. Dyka, C., Ingel, R.. An approach for tension instability in smoothed particle hydrodynamics (sph). *Computers & structures* 1995;57(4):573–580.

26. Zhang, C., Hu, X.Y., Adams, N.A.. A generalized transport-velocity formulation for smoothed particle hydrodynamics. *Journal of Computational Physics* 2017;337:216–232.

27. Adami, S., Hu, X., Adams, N.A.. A transport-velocity formulation for smoothed particle hydrodynamics. *Journal of Computational Physics* 2013;241:292–307.

28. Adepu, D., Ramachandran, P.. A corrected transport-velocity formulation for fluid and structural mechanics with sph. *arXiv preprint arXiv:210600756* 2021;.

29. Cleary, P.W.. Elastoplastic deformation during projectile–wall collision. *Applied Mathematical Modelling* 2010;34(2):266–283.

30. Yan, R., Bi, Y.q., Jiang, W.. Simulation of contact interface between elastic solids using smoothed particle hydrodynamics. *Computational Particle Mechanics* 2021;:1–11.

31. Vyas, D.R., Cummins, S.J., Rudman, M., Cleary, P.W., Delaney, G.W., Khakhar, D.V.. Collisional sph: A method to model frictional collisions with sph. *Applied Mathematical Modelling* 2021;94:13–35.

32. Mohseni-Mofidi, S., Drescher, E., Kruggel-Emden, H., Teschner, M., Bierwisch, C.. Particle-based numerical simulation study of solid particle erosion of ductile materials leading to an erosion model, including the particle shape effect. *Materials* 2021;15(1):286.

33. Ramachandran, P.. automan: A python-based automation framework for numerical computing. *Computing in Science & Engineering* 2018;20(5):81–97. doi:10.1109/MCSE.2018.05329818.

34. Monaghan, J.J.. Smoothed particle hydrodynamics. *Reports on progress in physics* 2005;68(8):1703.

35. Huang, C., Long, T., Li, S., Liu, M.. A kernel gradient-free SPH method with iterative particle shifting technology for modeling low-Reynolds flows around airfoils. *Engineering Analysis with Boundary Elements* 2019;106:571–587. doi:10.1016/j.enganabound.2019.06.010.

36. Thornton, C., Cummins, S.J., Cleary, P.W.. An investigation of the comparative behaviour of alternative contact force models during elastic collisions. *Powder Technology* 2011;210(3):189–197.

37. Guilkey, J.E., Bardenhagen, S., Roessig, K., Brackbill, J., Witzel, W., Foster, J.. Improved contact algorithm for the material point method and application to stress propagation in granular material 2001;.

38. de Vaucorbeil, A., Nguyen, V.P.. Modelling contacts with a total lagrangian material point method. *Computer Methods in Applied Mechanics and Engineering* 2021;373:113503.